Semi-supervised Invertible DeepONets for Bayesian Inverse Problems

Sebastian Kaltenbach¹, Paris Perdikaris² and Phaedon-Stelios Koutsourelakis^{1,3*}

¹Professorship of Data-driven Materials Modeling, School of Engineering and Design, Technical University of Munich, Boltzmannstr. 15, Garching, 85748, Germany.

²Department of Mechanical Engineering and Applied Mechanics, University of Pennsylvania, Philadelphia, 19104, USA.

³ Munich Data Science Institute (MDSI - Core member), www.mdsi.tum.de.

*Corresponding author(s). E-mail(s): p.s.koutsourelakis@tum.de; Contributing authors: sebastian.kaltenbach@tum.de; pgp@seas.upenn.edu;

Abstract

Deep Operator Networks (DeepONets) offer a powerful, data-driven tool for solving parametric PDEs by learning operators, i.e. maps between infinite-dimensional function spaces. In this work, we employ physics-informed DeepONets in the context of high-dimensional, Bayesian inverse problems. Traditional solution strategies necessitate an enormous, and frequently infeasible, number of forward model solves, as well as the computation of parametric derivatives. In order to enable efficient solutions, we extend DeepONets by employing a realNVP architecture which yields an invertible and differentiable map between the parametric input and the branch net output. This allows us to construct accurate approximations of the full posterior which can be readily adapted irrespective of the number of observations and the magnitude of the observation noise. As a result, no additional forward solves are required, nor is there any need for costly sampling procedures. We demonstrate the efficacy and accuracy of the proposed methodology in the context of inverse problems based on a anti-derivative, a reaction-diffusion and a Darcy-flow equation.

Keywords: DeepONets, Invertible architectures, Bayesian Inverse Problems, Semi-supervised Learning

1 Introduction

Nonlinear Partial Differential Equations (PDEs) depending on high- or even infinite-dimensional parametric inputs are ubiquitous in applied physics and engineering and appear in the context of several problems such as model calibration and validation or model-based design/optimization/control. In all these cases, they must be solved repeatedly for different values of the input parameters which poses an often insurmountable

obstacle as each of these simulations generally implies a significant computational cost. An obvious way to overcome these difficulties is to develop less-expensive but accurate surrogates which can be used on their own or in combination with a reduced number of runs of the high-fidelity, expensive, reference solver. The construction of such surrogates has been based on physical/mathematical considerations or data i.e. input-output pairs (and sometimes derivatives). Our contribution belongs to the latter category

of data-driven surrogates which has attracted a lot of attention in recent years due to the significant progress in the fields of statistical or machine learning (Koutsourelakis et al (2016)). We emphasize however that unlike typical supervised learning problems in data sciences, in the context of computational physics there are several distinguishing features. Firstly, surrogate construction is by definition a Small (or smallest possible) Data problem. The reason we want to have a surrogate in the first place is to avoid using the reference solver which is the one that generates the training data. Secondly, pertinent problems are rich in domain knowledge which should be incorporated as much as possible, not only in order to reduce the requisite training data but also to achieve higher predictive accuracy particularly in out-of-distribution settings. In the context of Bayesian inverse problems which we investigate in this paper, one does not know a priori where the posterior might be concentrated in the parametric space and cannot guarantee that all such regions will be sufficiently represented in the training dataset. Nevertheless the surrogate learned must be accurate enough in these regions in order to resolve the sought posterior.

Data-driven surrogates which are trained in an offline phase and are subsequently used for various downstream tasks have attracted a lot of attention in recent years (Bhattacharya et al, 2020). Most of these surrogates are constructed by learning a non-linear operator, e.g. a mapping between function spaces and thus between the inputs and the outputs of the PDE, which may or may not depend on additional input parameters. Notable methods that are learning such a nonlinear operator for PDEs include methods based on Deep Learning such as Physics-informed Neural Networks (PINNs) (Lagaris et al, 1998; Raissi et al, 2019) as well as the DeepONet architecture (Lu et al, 2021; Wang et al, 2021), which in contrast to PINNS not only takes the spatial and temporal location as an input but also accounts for input parameters of the PDE such as the viscosity in the Navier-Stokes equation. Moreover, Fourier Neural Networks (Li et al, 2020) have shown promising results by parametrizing the integral kernel directly in Fourier Space and thus restricting the operator to a convolution and the Learning Operators with Coupled Attention

(LOCA) framework (Kissas et al, 2022) builds upon the well-known attention mechanism that has already shown promising result in natural language processing.

We note that all of the Deep Learning frameworks mentioned fulfill the universal approximation theorem and, under certain conditions, can approximate the non-linear operator to arbitrary accuracy. Another possible framework without using Deep Learning is Optimizing a Discrete Loss (ODIL) Karnakov et al (2022) which was shown to be faster than PINNs due to the reduced number of parameters necessary but only obtains the solution on a discrete grid.

Besides the already mentioned surrogate models, time-dependent PDEs can also be approximated by methods based on Koopman operator theory (Koopman, 1931) which identify a transformation of the original systems that yield linear dynamics (Klus et al, 2018). As the dynamics is restricted to be linear, these methods (Lee and Carlberg, 2020; Gin et al, 2019; Champion et al, 2019) usually require a comparable large set of reduced order variables or an effective encoder/decoder structure. Especially for physical system, restricted dynamics for the reduced order variables can be used to ensure stability and deliver additional insight into the system (Kaltenbach and Koutsourelakis, 2021; Kalia et al, 2021; Kaltenbach and Koutsourelakis, 2020).

A common limitation of the aforementioned architectures is that they learn usually only the forward operator whereas for the solution of an inverse problem, its inverse would be most useful. In this work, we extend the DeepONet framework by replacing parts of its current neural network architecture with an invertible architecture. This allows one to perform both forward and inverse passes with the same neural network and the forward and inverse operators can be learned simultaneously. In particular, we make use of the RealNVP architecture (Dinh et al, 2016) which has an analytical inverse.

Furthermore we make use of both labeled and unlabeled (i.e. only inputs and residuals) training data in a physics-aware, semi-supervised approach. Whereas the use of labeled training data is straight-forward, unlabeled training data are incorporated by using the governing equations for these inputs and minimizing the

residuals similar to the physics-informed Deep-ONet (Wang et al, 2021). We note that it is easier and less-expensive to procure unlabeled data in comparison to labeled ones which leads to significant efficiency gains. Even though our algorithm can produce accurate predictions without any labeled training data and by only using a physics-informed loss, the addition of labeled training data can be used to improve the results. Finally, we show that the proposed invertible DeepONet can be used to very efficiently solve Bayesian inverse problems, i.e. to approximate the whole posterior distribution, without any need for multiple likelihood evaluations as required by alternative inference schemes such as Markov Chain Monte Carlo (MCMC, Beskos et al (2017)) or Sequential Monte Carlo (SMC, Koutsourelakis (2009)) or Stochastic Variational Inference (SVI, Detommaso et al (2018)). This makes our surrogate especially useful for Bayesian inverse problems. Whereas Deep Learning has been successfully applied to inverse problems before (Adler and Oktem, 2017; Ardizzone et al, 2018), our work differs by making use of a fully invertible operator learning architecture and being able to obtaining a posterior distribution for inverse problems.

The rest of the paper is structured as follows. In section 2 we review the basic elements of invertible NNs and DeepoNets and subsequently illustrate how these can be combined and trained with labeled and unlabeled. Furthermore we present how the resulting invertible DeepONet can be employed in order to approximate the posterior of a model-based, Bayesian inverse problem at minimal additional cost. We demonstrate features and assess the performance of the proposed methodology in section 3 where it is applied to a reactiondiffusion PDE and the Darcy problem. The cost and accuracy of the posterior approximation in the context of pertinent Bayesian inverse problems are demonstrated in section 3.4. Finally, we conclude in section 4 with a summary of the main findings and a discussion on the (dis)advantages of the proposed architecture and potential avenues for improvements.

2 Methodology

We first review some basic concepts of invertible neural networks and DeepONets. We subsequently present our novel contributions which consist of an invertible DeepONet architecture and its use for solving efficiently Bayesian inverse problems.

2.1 Invertible Neural Networks

Neural Networks are in general not invertible which restricts their application in problems requiring inverse operations. Invertibility can be achieved by adding a momentum term (Sander et al, 2021), restricting the Lipschitz-constant of each layer to be smaller than one (Behrmann et al., 2019) or using special building blocks (Dinh et al, 2016). These formulations have primarily been developed for flow-based architectures but we will apply them to operator learning within this work. We choose realNVP (Dinh et al, 2016) as this architecture enables an analytical inverse which ensures efficient computations. Each RealNVP building block consists of the transformation below which includes two neural networks denoted by k(.) and r(.). Given a D dimensional input $\boldsymbol{x} = \{x_i\}_{i=1}^D$ of an invertible layer and d < D, the output $\mathbf{y} = \{y_i\}_{i=1}^D$ is obtained as follows:

$$y_{1:d} = x_{1:d} (1)$$

$$y_{d+1:D} = x_{d+1:D} \circ exp(k(x_{1:d})) + r(x_{1:d})$$
 (2)

Here, \circ is the Hadamard or element-wise product and d is usually chosen to be half of the dimension of the input vector i.e. d = D/2.

As only d of the components are updated, the input entries after each building block are permuted, e.g. we reverse the vector after one building block to ensure that after a second building block all of them are modified. Therefore, at least two building blocks are needed in order to modify all entries. We note, that the dimension of the input cannot change and needs to be identical to the dimension of the output. The two neural networks involved can consist of arbitrary layers as long as their output and input dimensions are consistent with Equation 2.

The maps defined can be easily inverted which leads to the following equations:

$$x_{1:d} = y_{1:d} (3)$$

$$x_{d+1:D} = (y_{d+1:D} - r(x_{1:d})) \circ exp(-k(x_{1:d}))$$
 (4)

We note that due to this structure, the Jacobian is diagonal and its determinant can be obtained by multiplying the diagonal entries only.

2.2 DeepONets

Before presenting our novel architecture for invertible DeepONets, we briefly review the original DeepONet formulation by Lu et al (2021). Deep-ONets have been developed to solve parametric PDEs and significantly extend the Physics-Informed Neural Network (PINNs, Raissi et al (2019)) framework as no additional training phase is required if the input parameters of the PDE are changed. We consider a, potentially nonlinear and time-dependent, PDE with an input function $u \in \mathcal{U}$ and solution function $s \in \mathcal{S}$ where \mathcal{U}, \mathcal{S} are appropriate Banach spaces. The former can represent e.g. source terms, boundary or initial conditions, material properties. Let:

$$\mathcal{N}(u, s)(\boldsymbol{\xi}) = 0 \tag{5}$$

denote the governing PDE where $\mathcal{N}: \mathcal{U} \times \mathcal{S} \to \mathcal{V}$ is an appropriate differential operator and $\boldsymbol{\xi}$ the spatio-temporal coordinates. Furthermore, let:

$$\mathcal{B}(u, s)(\boldsymbol{\xi}) = 0 \tag{6}$$

denote the operator $\mathcal{B}: \mathcal{U} \times \mathcal{S} \to \mathcal{V}$ associated with the boundary conditions. Assuming that the solution s for each $u \in \mathcal{U}$ is unique, we denote with $\mathcal{G}:\mathcal{U}\to\mathcal{S}$ the solution operator that maps from any input u to the corresponding solution s, the goal of DeepONets is to approximate it with an operator G_{θ} that depends on tunable parameters $\boldsymbol{\theta}$. The latter can yield an approximation to the actual solution at any spatio-temporal point $\boldsymbol{\xi}$ which we denote by $G_{\boldsymbol{\theta}}(\boldsymbol{\xi})$. It is based on a separated representation (Lu et al, 2021):

$$G_{\boldsymbol{\theta}}(u)(\boldsymbol{\xi}) = \sum_{i=1}^{Q} b_i \left(\underbrace{u(\boldsymbol{\eta}_1), ..., u(\boldsymbol{\eta}_F)}_{\boldsymbol{\eta}} \right) t_i(\boldsymbol{\xi})$$
(7)

and consists of the so-called branch network whose terms b_i depend on the values of the input

function u at F fixed points $\{\eta_j\}_{j=1}^{F-1}$ which we summarily denote with the vector $\boldsymbol{u} \in \mathbb{R}^F$, and the so-called trunk network whose terms t_i depend on the spatio-temporal coordinates ξ . Both networks have trainable weight and bias parameters which we denote collectively by θ .

We note that in the next section, we will use a vectorized formulation of Equation (7) and process various spatio-temporal coordinate data points together as this is needed to ensure invertibility of the DeepONet. Labeled data can be used for training which consist of pairs of u and corresponding solutions s = G(u) evaluated at certain spatio-temporal locations. Unlabeled training data (i.e. only inputs) can also be employed in a physics-informed approach as introduced by Wang et al (2021), by including the governing PDE in Equation (5) in an additional loss term as discussed section 2.4.

2.3 Invertible DeepONets

The invertible RealNVP introduced in section 2.1 is employed exclusively on the branch network i.e. we assume that:

$$D = F = Q \tag{8}$$

and the input x of section 2.1 is the vector $u \in \mathbb{R}^F$ containing the values of the PDE input at D = Fspatio-temporal locations whereas the output y of section 2.1 is now the D = Q values of the branch net $\boldsymbol{b} \in \mathbb{R}^D$. We note that this restriction regarding the equality of the dimension of the input uand the output b is due to the use of an invertible architecture. Fortunately we can choose the dimension of b freely as together with the branch network we simultaneously train the trunk network whose output weighs each component of bbefore calculating the final solution.

In view of the inverse problems we would like to address, we consider the PDE solution at K spatio-temporal locations, $\{\boldsymbol{\xi}_k\}_{k=1}^K$ and we denote with $\boldsymbol{s} \in \mathbb{R}^K$ the vector containing the PDE solution values at these locations i.e. s = $[s(\boldsymbol{\xi}_1),\ldots,s(\boldsymbol{\xi}_K)]^T$. Finally we denote with \boldsymbol{Y}

¹These points are usually chosen to be uniformly distributed over the entire domain, but it is also possible to increase their density in certain areas, e.g. with high variability.

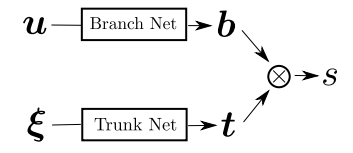


Fig. 1 DeepONet architecture

the $K \times D$ matrix constructed by the values of the trunk network outputs at the aforementioned locations, i.e.:

$$\boldsymbol{Y} = \begin{bmatrix} t_1(\boldsymbol{\xi}_1) & \dots & t_D(\boldsymbol{\xi}_1) \\ \dots & \dots & \dots \\ t_1(\boldsymbol{\xi}_K) & \dots & t_D(\boldsymbol{\xi}_K) \end{bmatrix}$$
(9)

As a result of Equation (7) we can write that:

$$s = Yb \tag{10}$$

As the matrix Y is in general non-invertible, one can determine b given s by solving a least-squares problem, i.e.:

$$\min_{\boldsymbol{b}} \mid \boldsymbol{s} - \boldsymbol{Y} \boldsymbol{b} \mid^2 \tag{11}$$

or a better-behaved, regularized version thereof:

$$\min_{\boldsymbol{b}} |\boldsymbol{s} - \boldsymbol{Y}\boldsymbol{b}|^2 + \epsilon |\boldsymbol{b}|^2 \tag{12}$$

where a small value is generally sufficient for the regularization parameter $\epsilon << 1$. We note that given s and once b has been determined by solving Equation (11) or Equation (12), we can make use of the invertibility of the branch net in order to obtain the input vector u. For the ensuing equations we denote the forward map implied by Equation (10) as:

$$s = \mathcal{F}_{\theta}(u, Y) \tag{13}$$

and the inverse obtained by the two steps described above as:

$$\boldsymbol{u} = \mathcal{I}_{\boldsymbol{\theta}}(\boldsymbol{s}, \boldsymbol{Y}) \tag{14}$$

Both maps output a vector based on the input u for the forward case and solution s in the inverse case and the matrix Y, e.g. the spatio-temporal

locations which are first processed by the trunk network.

2.4 A Semi-supervised Approach for Invertible DeepONets

As mentioned earlier and in order to train the invertible DeepONet proposed, i.e. to find the optimal values for the parameters θ , we employ both labeled (i.e pairs of PDE-inputs u and PDE-outputs s) and unlabled data (i.e. only PDE-inputs u) in combination with the governing equations. The loss function L employed is therefore decomposed into two parts as:

$$L = L_{labeled} + L_{unlabeled} \tag{15}$$

The first part $L_{labeled}$ employs the labeled data and is further decomposed as:

$$L_{labeled} = L_{l,forward} + L_{l,inverse}$$
 (16)

Without loss of generality and in order to keep the notation as simple as possible we assume N_l pairs of labeled data are available, each of which consists of the values of PDE-input at D locations which we denote with $\mathbf{u}^{(i)} \in \mathbb{R}^D$, $i = 1, \dots N_l$ and the values of the PDE-output at K spatiotemporal locations which we denote with $\mathbf{s}^{(i)} \in \mathbb{R}^K$, $i = 1, \dots N_l$. If the $K \times D$ matrix \mathbf{Y}^2 is defined as in Equation (9) and in view of the forward (Equation (13)) and inverse (Equation (14)) maps defined earlier, we can write that:

$$L_{l,forward} = \frac{1}{N_l} \sum_{i=1}^{N_l} | \boldsymbol{s}^{(i)} - \mathcal{F}_{\boldsymbol{\theta}}(\boldsymbol{u}^{(i)}, \boldsymbol{Y}) |^2 \quad (17)$$

 $^{^2}$ In general, the matrix Y could contain different spatiotemporal locations for each PDE-input $u^{(i)}$ and solution $s^{(i)}$ but for simplicity reasons we drop the index i here.

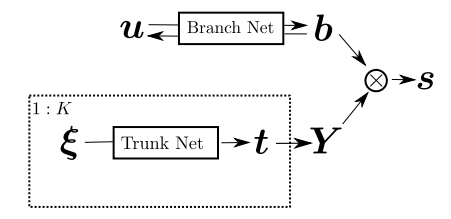


Fig. 2 Invertible DeepONet architecture

and:

$$L_{l,inverse} = \frac{1}{N_l} \sum_{i=1}^{N_l} | \boldsymbol{u}^{(i)} - \mathcal{I}_{\boldsymbol{\theta}}(\boldsymbol{s}^{(i)}, \boldsymbol{Y}) |^2 \quad (18)$$

By employing both loss terms, the optimal parameters θ can balance the accuracy of the approximation in both maps.

Furthermore and assuming N_u PDE-inputs are available each of which is evaluated at D spatiotemporal points $\{\boldsymbol{\xi}^{(i)}\}_{i=1}^D$ with $\boldsymbol{u}^{(i)} \in \mathbb{R}^D$ denoting these values, we express the $L_{unlabeled}$ loss term as:

$$L_{unlabeled} = L_{BC} + L_{res} + L_{u,inverse}$$
 (19)

The first L_{BC} and second L_{res} term are physics-informed Wang et al (2021) and account for the residuals in the boundary (and/or initial) conditions and the governing PDE respectively. In the case of L_{BC} we select N_B (uniformly distributed) points along the boundary, say $\boldsymbol{\xi}_B^{(j)}$, $j=1,\ldots,N_B$. Then, in view of Equation (6), we employ:

$$L_{BC} = \frac{1}{N_u N_B} \sum_{i=1}^{N_u} \sum_{j=1}^{N_B} |\mathcal{B}(u^{(i)}, G_{\theta}(u^{(i)}))(\boldsymbol{\xi}_B^{(j)})|^2$$
(20)

In the interior of the problem domain and in view of Equation (5), we employ a loss:

$$L_{res} = \frac{1}{N_u N_{res}} \sum_{i=1}^{N_u} \sum_{j=1}^{N_{res}} |\mathcal{N}(u^{(i)}, G_{\theta}(u^{(i)})(\boldsymbol{\xi}^{(j)})|^2$$
(21)

which involves N_{res} collocation points.

The third term $L_{u,inverse}$ pertains to the forward and inverse maps in Equations (13), (14) and

can be expressed as:

$$L_{u,inverse} = \frac{1}{N_u} \sum_{i=1}^{N_u} | \boldsymbol{u}^i - \mathcal{I}_{\boldsymbol{\theta}}(\mathcal{F}_{\boldsymbol{\theta}}(\boldsymbol{u}^{(i)}, \boldsymbol{Y}), \boldsymbol{Y})) |^2$$
(22)

where the matrix Y is defined as in Equation (9).

The minimization of the combined loss L with respect to the network parameters θ of the branch and trunk network is performed with stochastic gradient descent and the ADAM (Kingma and Ba, 2014) scheme in particular. Gradients of the loss were computed using the automatic differentiation tools of the JAX library (Bradbury et al, 2018). We finally note that the D spatioemporal locations need not be the same nor do they need to be equal in number in all data instances as assumed in the equations above. In such cases the vector of the observables and the matrices Y involved would differ which would further complicate the notation but the same DeepONet parameters θ would appear in all terms.

2.5 Semi-supervised, invertible DeepONets for Bayesian inverse problems

In this section we discuss how the invertible Deep-ONets proposed and trained as previously discussed, can be used to efficiently approximate the solution of a Bayesian inverse problem in the presence of, potentially noisy, observations as well as prior uncertainty about the unknowns. A central role is played by the readily available invertible map which the RealNVP architecture affords. In particular, let $\hat{s} \in \mathbb{R}^K$ denote a vector of noisy observations of the PDE-solution at certain K spatio-temporal locations. These are assumed to be related to the PDE-solution's values at these locations, denoted summarily by $s \in \mathbb{R}^K$, as

follows:

$$\hat{s} = s + \sigma \, \eta, \qquad \eta \sim \mathcal{N}(0, I).$$
 (23)

where σ^2 is the noise variance. This in turn defines a conditional density $p(\hat{s} \mid s)$:

$$p(\hat{\boldsymbol{s}} \mid \boldsymbol{s}) = \mathcal{N}(\hat{\boldsymbol{s}} \mid \boldsymbol{s}, \sigma^2 \boldsymbol{I}). \tag{24}$$

By combining this with Equation (10), we can obtain a conditional density (likelihood) on $b \in \mathbb{R}^D$, i.e. the D-dimensional, branch-network output vector b of the form:

$$p(\hat{\boldsymbol{s}} \mid \boldsymbol{s}) = \mathcal{N}(\hat{\boldsymbol{s}} \mid \boldsymbol{Y} \boldsymbol{b}, \sigma^2 \boldsymbol{I}). \tag{25}$$

Our goal is to determine the D-dimensional, PDE-input vector \boldsymbol{u} , or better yet the posterior thereof. Let $p_{\boldsymbol{u}}(\boldsymbol{u})$ denote the selected prior on $\boldsymbol{u} \in \mathbb{R}^D$ which is related to \boldsymbol{b} through the invertible RealNVP. This implies a prior density $p_{\boldsymbol{b}}(\boldsymbol{b})$ which is given by:

$$p_b(\mathbf{b}) = p_u(\mathbf{b}_{NN}^{-1}(\mathbf{b})) \ J(\mathbf{b}) \tag{26}$$

where $b_{NN}: \mathbb{R}^D \to \mathbb{R}^D$ denotes the invertible map learned between \boldsymbol{u} and \boldsymbol{b} , \boldsymbol{b}_{NN}^{-1} is its inverse and $J(\boldsymbol{b}) = |\frac{\partial \boldsymbol{b}_{NN}^{-1}}{\partial \boldsymbol{b}}|$ is the determinant of its Jacobian. The latter, as mentioned in section 2.1, is a diagonal matrix and its determinant can be readily computed at a cost $\mathcal{O}(D)$.

Given the prior $p_u(\mathbf{u})$, we first construct an approximation $p_{b,G}(\mathbf{b})$ of $p_b(\mathbf{b})$ with a mixture of D-dimensional Gaussians, i.e.:

$$p_{b,G}(\boldsymbol{b}) = \sum_{m=1}^{M} w_j \, \mathcal{N}(\boldsymbol{b} \mid \boldsymbol{m}_{b,m}, \boldsymbol{S}_{b,m})$$
 (27)

where M denotes the number of mixture components. Such an approximation can be readily computed, e.g. using Variational Inference (Hoffman et al, 2013) and without any forward or inverse model evaluations by exploiting the fact that samples from p_b can be readily drawn using ancestral sampling i.e. by drawing samples of \boldsymbol{u} from p_u and propagating those with b_{NN} .

By combining the (approximate prior) $p_{b,G}(\mathbf{b})$ above with the Gaussian likelihood $p(\hat{\mathbf{s}} \mid \mathbf{b})$ of Equation (25) we obtain a closed-form posterior $\tilde{p}(\mathbf{b} \mid \hat{\mathbf{s}})$ on \mathbf{b} which also consists of a mixture of

Gaussians of the form:

$$\tilde{p}(\boldsymbol{b} \mid \hat{\boldsymbol{s}}) = \sum_{m=1}^{M} \tilde{w}_{j} \, \mathcal{N}(\boldsymbol{b} \mid \boldsymbol{\mu}_{b,m}, \boldsymbol{C}_{b,m})$$
 (28)

where:

$$C_{b,m}^{-1} = \sigma^{-2} Y^{T} Y + S_{b,m}^{-1}$$

$$C_{b,m}^{-1} \mu_{b,m} = \sigma^{-2} Y^{T} \hat{s} + S_{b}^{-1} m_{b,m}$$
(29)

The weights \tilde{w}_m $(\sum_{m=1}^M \tilde{w}_m = 1)$ would be proportional to:

$$\tilde{w}_m \propto w_m \mid \boldsymbol{D}_m \mid^{-1/2} \exp(-\frac{1}{2}(\hat{\boldsymbol{s}} - \boldsymbol{Y} \boldsymbol{m}_{b,m})^T \\ \boldsymbol{D}_m^{-1}(\hat{\boldsymbol{s}} - \boldsymbol{Y} \boldsymbol{m}_{b,m}))$$
(30)

where:

$$\boldsymbol{D}_{m} = \sigma^{2} \boldsymbol{I} + \boldsymbol{Y} \boldsymbol{S}_{h \, m} \boldsymbol{Y}^{T} \tag{31}$$

Therefore inference tasks can be readily carried out by sampling \boldsymbol{b} from the mixture-of-Gaussians posterior above and propagating those samples through the inverse map b_{NN}^{-1} to obtain \boldsymbol{u} -samples. We note finally that the accuracy of the approximation can be assessed with Importance Sampling which would nevertheless imply additional, full-order model runs.

3 Numerical Illustrations

We applied the proposed framework to three examples, i.e. the antiderivate operator, a reaction-diffusion PDE as well as a Darcy-type elliptic PDE. In each of these cases, we report the relative errors of forward and inverse maps (on test data) when trained with varying amounts of labeled and unlabeled training data. For the reaction-diffusion PDE and the Darcy-type elliptic PDE, we also use our invertipble-DeepONetsurrogate to solve pertinent Bayesian inverse problems. The code for the aforementioned numerical illustrations is available here³.

3.1 Anti-derivative Operator

As a first test case we considered the antiderivative operator on the Interval $\xi = y \in [0, 1]$ with:

$$\frac{ds(\xi)}{d\xi} = u(\xi) \text{ with } s(0) = 0 \tag{32}$$

i.e. when the input u corresponds to the right-hand-side of this ODE and the operator G(u) that we attempt to approximate is simply the integral operator $G(u)(\xi) = \int_0^{\xi} u(t) dt$. We generated $N_u = 10000$ unlabeled training data by sampling inputs u from a Gaussian process with zero mean and exponential quadratic covariance kernel with a length scale l = 0.2. Their values at the same D = 100 uniformly-distributed locations in [0,1] were recorded. We subsequently randomly choose $N_{res} = 200$ collocation points to evaluate the residuals (see Equation (21)).

Moreover, we used up to $N_l = 10000$ labeled training data, for which the inputs were generated similar as for the unlabeled training data, and the outputs were obtain by solving the ODE above. We trained the invertible DeepONet on $N_u = 10000$ unlabeled training data with a batch size of 100. In each batch we added 1, 10 or 100 labeled training data points per batch (i.e. $N_l = 100, 1000, 10000$ respectively in Equations (17), (18)). A minimum of one labeled datapoint is required in order to set the boundary condition correctly as for this stationary problem we did not enforce the boundary conditions separately in the

Using the ADAM optimizer and an initial learning rate of 0.001, we run the model training for 40000 iterations with an exponential learning rate decay with rate 0.9 every 1000 iterations. As test data, we used 1000 new (i.e. not be seen during training) input-output pairs and compared the predicted forward and inverse solutions with the actual ones. The results obtained in terms of the relative errors are summarized in Table 1.

The error values indicate that both the forward as well as the inverse maps are very well approximated by our invertible DeepONet. The addition of more labeled training data results in even lower errors especially for the inverse map for which the relative error is decreased from almost $\sim 4\%$ to $\sim 2\%$.

In order to visualize the results we plot for four randomly-chosen test cases the predictions (when trained with 10% labeled data) of both the forward (Figure 3) and inverse (Figure 4) operator. In all cases, the predictions are indistinguishable from the reference functions.

In Appendix A we included results of the simulation described here with varying amounts of unlabeled and labeled training data to show the influence of the amount of training data on the result.

unlabeled loss part. With regards to the architecture of the networks used, we employed a MLP with four layers and 100 neurons each for the trunk network and 6 RealNVP building blocks for the branch network which were parametrized by a two-layered MLP. Variations around these values in the number of neurons, layers were also explored and did not impact significantly the performance.

 $^{^3\}mathrm{URL}$ will be added upon publication

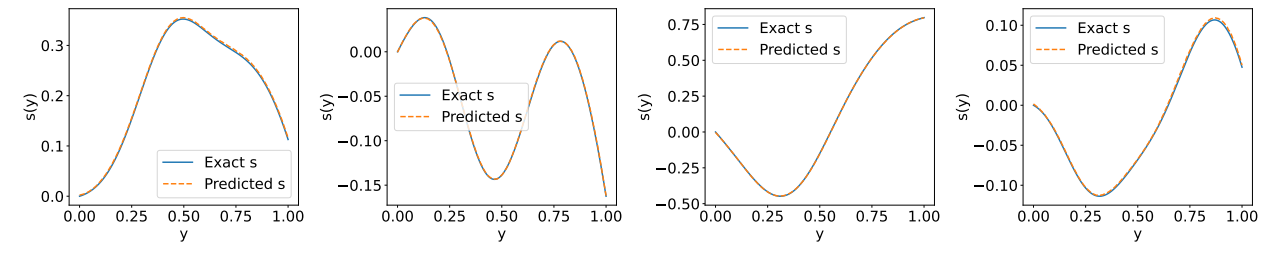


Fig. 3 Forward map - Comparison of the true PDE-output/solution s (given a PDE-input u) with the one predicted by the proposed invertible DeepONet and for the anti-derivative operator

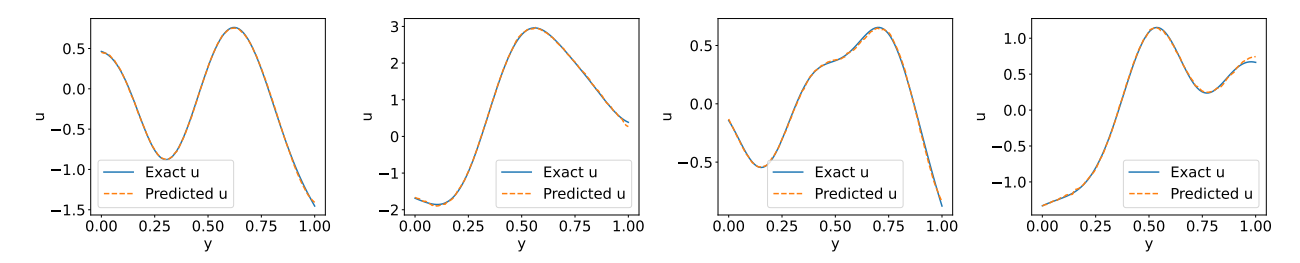


Fig. 4 Inverse map - Comparison of the true PDE-input u (given the PDE-output/solution s) with the one predicted by the proposed invertible DeepONet and for the anti-derivative operator

3.2 Reaction-Diffusion

The second illustrative example involved the reaction-diffusion equation on the space-time domain $\boldsymbol{\xi}=(x,t)\in[0,1]\times[0,1]$:

$$\frac{\partial s}{\partial t} = D_s \frac{\partial^2 s}{\partial x^2} + ks^2 + u(x) \tag{33}$$

Here, $D_s=0.01$ is the diffusion constant and k=0.01 is the reaction rate and the source-term u(x) is chosen to be the PDE-input. We used zero values as initial conditions and boundary conditions. We generated random source terms by sampling from a Gaussian process with zero mean and and exponential quadratic covariance kernel with a length scale l=0.2 which were then evaluated at D=100 uniformly distributed points over [0,1]. The PDE was subsequently solved using an implicit Finite-Difference scheme.

We trained our model based on $N_u=5000$ unlabeled training data points and added varying amounts of labeled training data to each batch of 100 unlabeled samples. Since for this problem the boundary conditions were enforced separately, the amount of labeled training data used can also be zero. All unlabeld training data points were evaluated at $N_{res}=200$ randomly selected collocation

points. With regards to the network architecture, we employed a MLP with five layers and 100 neurons each for the trunk network and 3 RealNVP building blocks for the branch network which were parametrized by a three-layered MLP. Using the ADAM optimizer and an initial learning rate of 0.001, we run the model training for 120000 iterations with an exponential learning rate decay with rate 0.9 every 2000 iterations. For our test dataset, we generated 1000 new (unseen) source terms u and corresponding solutions s. A summary of the relative errors obtained is contained in Table 2.

We note that again for all three settings we achieve very low error rates, which decrease as the amount of labeled training data increases. In Figure 5 and 6 we show the predictions (trained with 10% labeled data) of both forward and inverse map for three randomly chosen test cases.

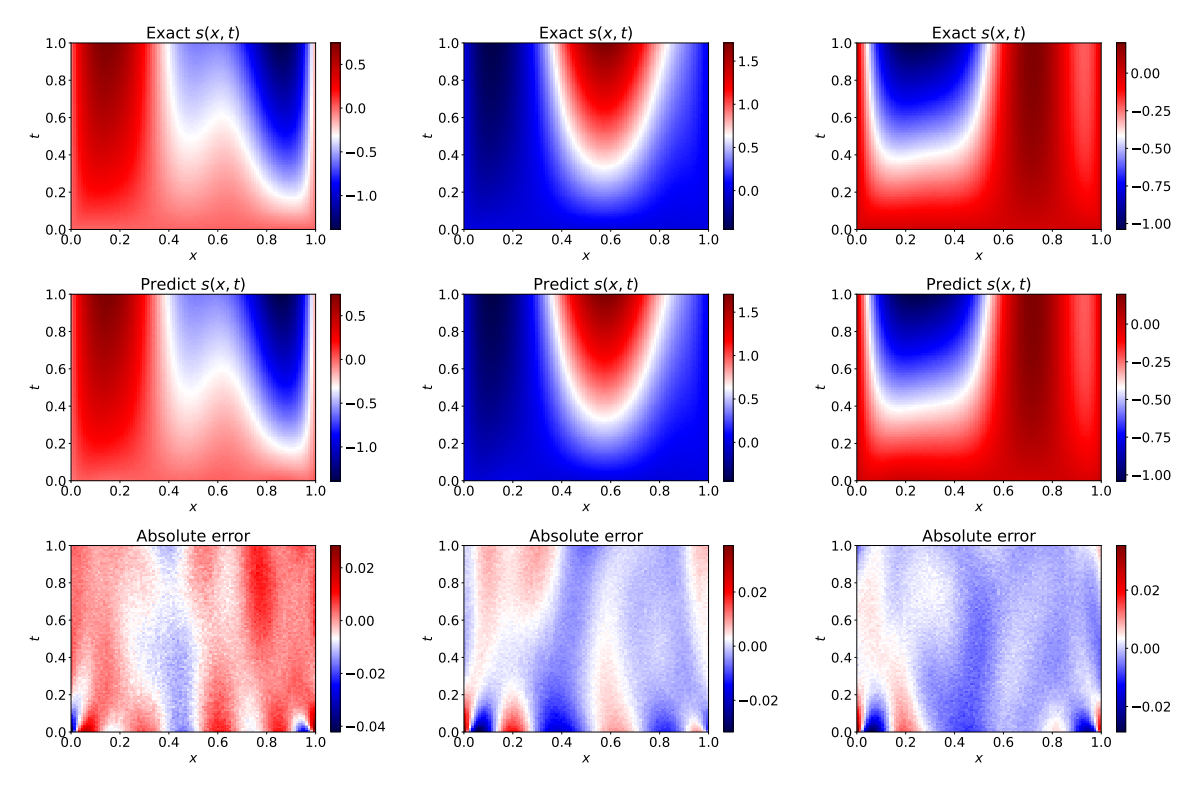


Fig. 5 Forward map - Comparison of the true PDE-output/solution s (given the PDE-input u) with the one predicted by the proposed invertible DeepONet and for Reaction-Diffusion PDE.

3.3 Darcy

In the final example we considered the Darcy equation on the two-dimensional domain $\boldsymbol{\xi} = (x_1, x_2) \in [0, 1]^2$

$$\nabla \cdot (u(\boldsymbol{\xi})\nabla s(\boldsymbol{\xi})) = 10 \tag{34}$$

where the PDE-input u corresponds to the diffusion coefficient field. We assumed zero values of s along all boundaries which we a-priori incorporated in our operator approximation by multiplying the DeepONet expansion in Equation (7) with the polynomial $x_1(1-x_1)$ $x_2(1-x_2)$. We used $N_u = 1000$ unlabeled training data points with $N_{res} = 3844$ collocation points (Equation (21)) during training and added either no labeled training data at all (i.e. $N_l = 0$) or $N_l = 1000$. To obtain the latter we solved Equation 34 with the Finite Element library FEniCS (Logg et al, 2012) on a 128×128 mesh with linear elements. We defined the PDE-inputs u to be coefficients of 64 feature functions, which are defined in Equation 35. To generate the training data, we sampled

each of the 64 coefficient c from a uniform random distribution and scaled the corresponding \sin/\cos functions with these coefficients. The field u was therefore parametrized as following.

$$\ln(u) = \sum_{f_1=1}^{4} \sum_{f_2=1}^{4} c_{f_1, f_2, 1} \sin(f_1 x_1) \cos(f_2 x_2)$$

$$+ c_{f_1, f_2, 2} \sin(f_1 x_1) \sin(f_2 x_2)$$

$$+ c_{f_1, f_2, 3} \cos(f_1 x_1) \sin(f_2 x_2)$$

$$+ c_{f_1, f_2, 4} \cos(f_1 x_1) \cos(f_2 x_2)$$
(35)

We note that we need to apply the exponential at the end in order to ensure that our diffusion coefficient field is positive.

With regards to the network architecture, we employed a MLP with five layers and 64 Neurons each for the trunk network and 3 RealNVP building blocks for the branch network which were parametrized by a three-layered MLP. Using the ADAM optimizer and an initial learning rate of

labeled data [%]		10	100
relative error s (forward map)	0.0152 ± 0.0151	$0.0152 \pm 0.0151 \mid 0.00791 \pm 0.00799 \mid 0.00152 \pm 0.00151 \mid 0.00791 \pm 0.00191 \mid 0.00151 \mid 0.0015$	0.00728 ± 0.00797
relative error u (inverse map)) 0.0371 ± 0.0241 0.034 ± 0.024	0.034 ± 0.024	0.0215 ± 0.0153
Table 1 Relative test errors and their	r standard deviations	depending on the amour	Table 1 Relative test errors and their standard deviations depending on the amount of labeled training data for the anti-derivative opera

Table 1 Relative test errors and their standard deviations depending on the amount or iappear training data, e.g. in the 10percent case we used ten times more unlabeled training data whereas in the 100percent case the amount of labeled and unlabeled training data was the same.

			-
100	relative error for s $\mid 0.00925 \pm 0.00492 \mid 0.0105 \pm 0.00519 \mid 0.00813 \pm 0.00445$	$0.024 \pm 0.01021 \mid 0.0184 \pm 0.00578 \mid 0.0162 \pm 0.00592$	M-11- 6 D-1-15
10	0.0105 ± 0.00519	0.0184 ± 0.00578	1-1 7- 7
0	0.00925 ± 0.00492	0.024 ± 0.01021	44 -4-4 - 1 1
labeled data [%]	relative error for s	relative error for u	

Table 2 Relative errors on test data depending on the amount of labeled training data for the reaction-diffusion case.

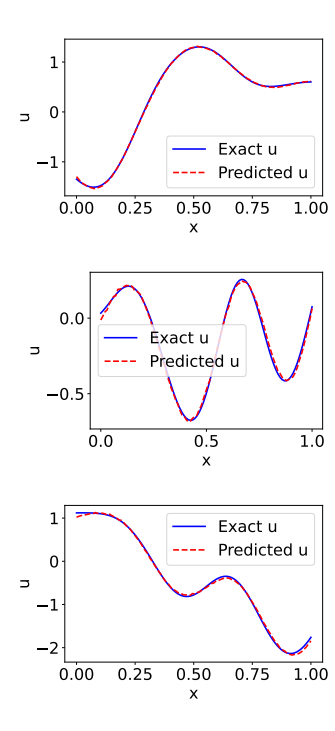


Fig. 6 Inverse map - Comparison of the true PDE-input u (given the PDE-output/solution s) with the one predicted by the proposed invertible DeepONet and for Reaction-Diffusion PDE.

0.001, we run the model training for 100000 iterations with an exponential learning rate decay with rate 0.9 every 2000 iterations.

We tested the learned model on 2500 unseen test data and obtained the results in Table 3.

In Figure 7 we compare the reference solution for two illustrative test cases with the the forward map learned with labeled training data. As suggested by the cumulative results Table 3 the two predictions are very close to the reference and the accuracy is very high.

In Figure 8 and 9 the results for two illustrative inverse test case are shown. Due to the large difference in accuracy for the cases with and without labeled training data in Table 3 we visualized the results for both cases. In Figure

8 the results are shown for the training without labeled data. Whereas the accuracy is lower for the case without labeled training data we are still able to identify the main characteristics for the parameter input despite its complex shape and a challenging inverse problem. For the case with the added labeled training data (Figure 9), the accuracy is higher. The model is for both cases able to identify the full parameter input field for unseen test data which is for both cases reconstructed using Equation 35 and the obtained coefficients. Therefore, we do not lose any information here due to a reduction of the dimension but the parametrization of the input field needs to be known a priori.

In case we are not able to define feature coefficients as inputs, this example poses an additional difficulty as the input, denoted by \boldsymbol{u} e.g. in section 2.3, generally needs to be high-dimensional to capture the variations in this two-dimensional field. Since the dimension of the branch-net's outputs needs to be the same in order to ensure invertibility, we then need to perform, a-priori, a dimensionality reduction to the input. An example is presented in the following subsection.

3.3.1 Coarse-grained (CG) input parameters

For this section, we generated our parameter input by sampling a Gaussian process with mean zero and exponential quadratic covariance with length scale l = 0.1. As the diffusion coefficient u must be positive everywhere, we applied the exponential function to the samples obtained. The resulting fine-grained field u on a 128×128 grid was used to generate the reference solution. We constructed a coarse-grained version of each u by considering its values on a 8×8 grid (i.e. by sub-sampling the fine-grained version), which we used as the input to the DeepONet and the branch network in particular. We generated $N_u = 1000$ unlabeled fields u in total and used $N_{res} = 3844$ collocation points (Equation (21)) during training. We also trained the model with $N_l = 1000$ labeled training

The results can be found in Table 4. The test data in this table consists of 2500 unseen, fine-grained, diffusion coefficient fields and their respective solutions. Even though good accuracy can be attained without labeled training data, its

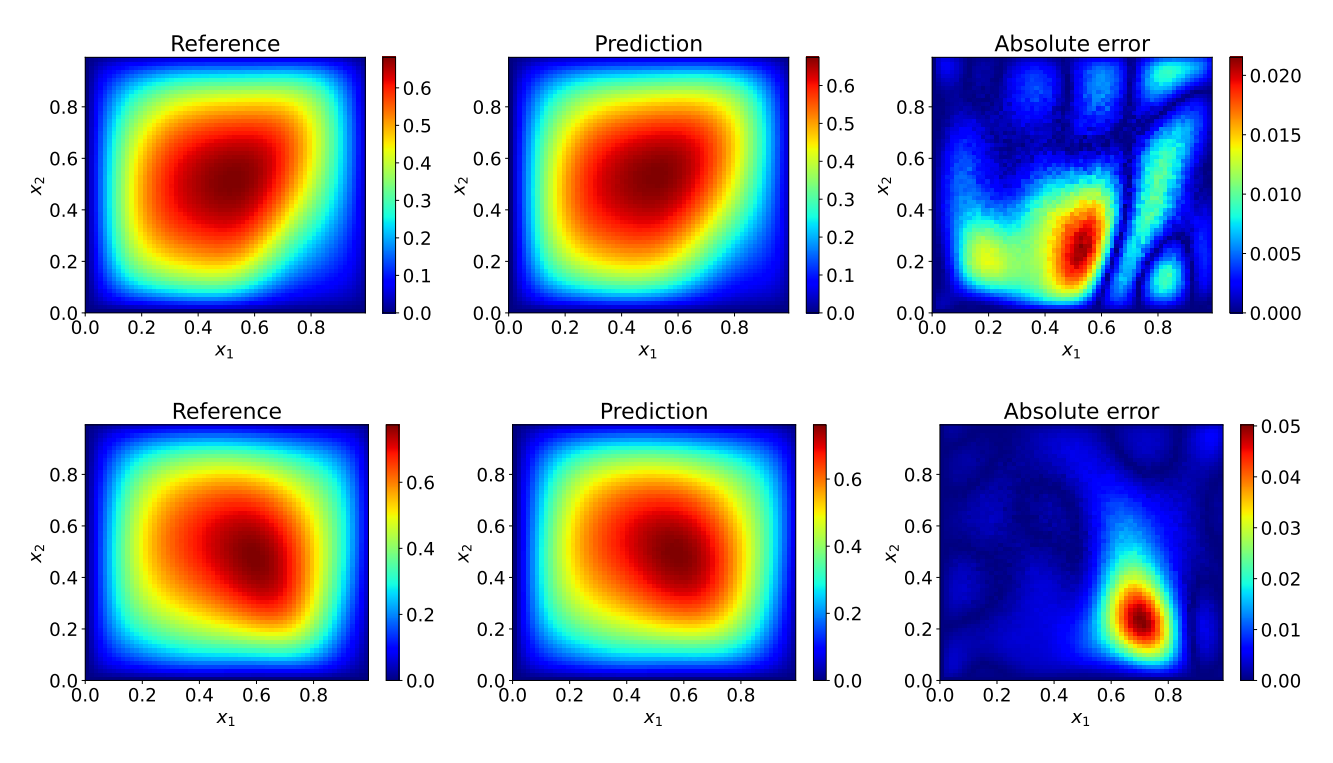


Fig. 7 Forward map - Comparison of the true PDE-output/solution s (given feature coefficients as the PDE-input u) with the one predicted by the proposed invertible DeepONet and for Darcy type PDE.

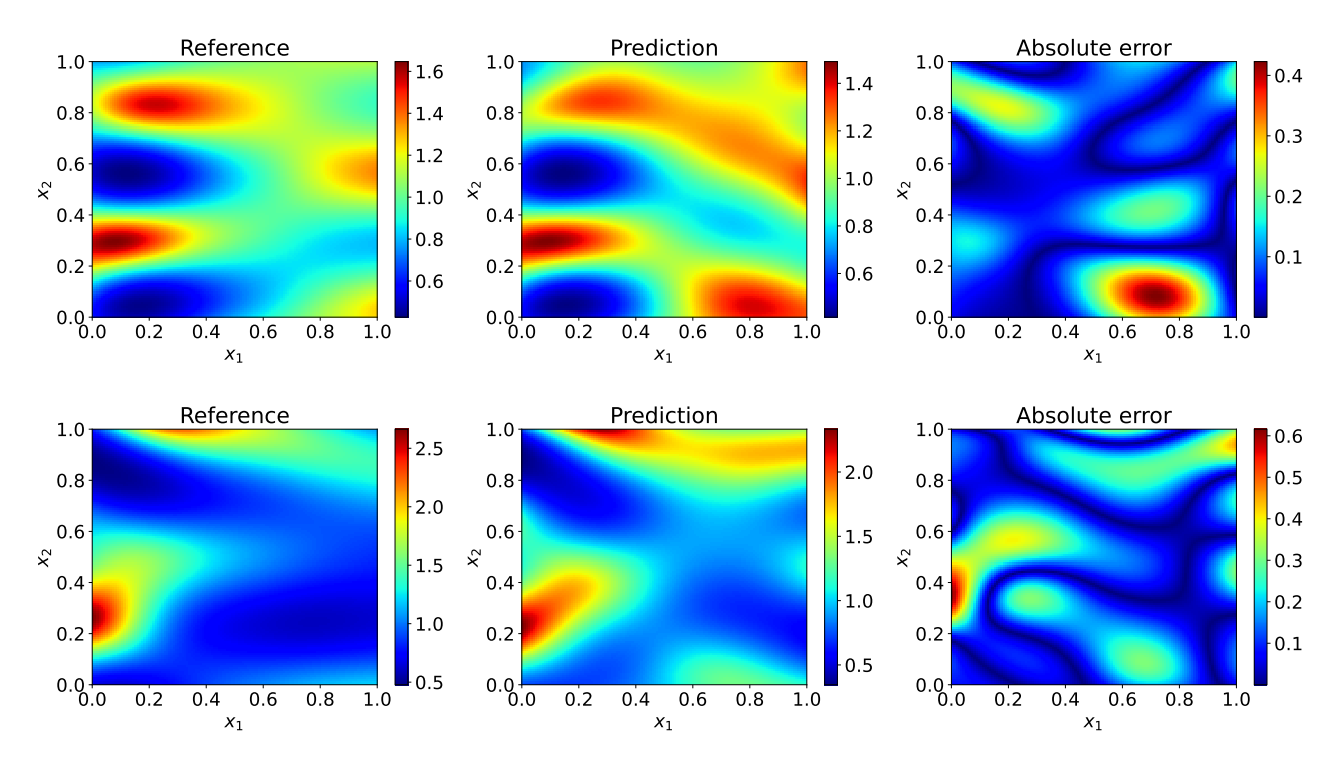


Fig. 8 Inverse map - Comparison of the reconstructed PDE-input (given the PDE-output/solution s) with the one predicted by the proposed invertible DeepONet and for Darcy type PDE with zero labeled training data.

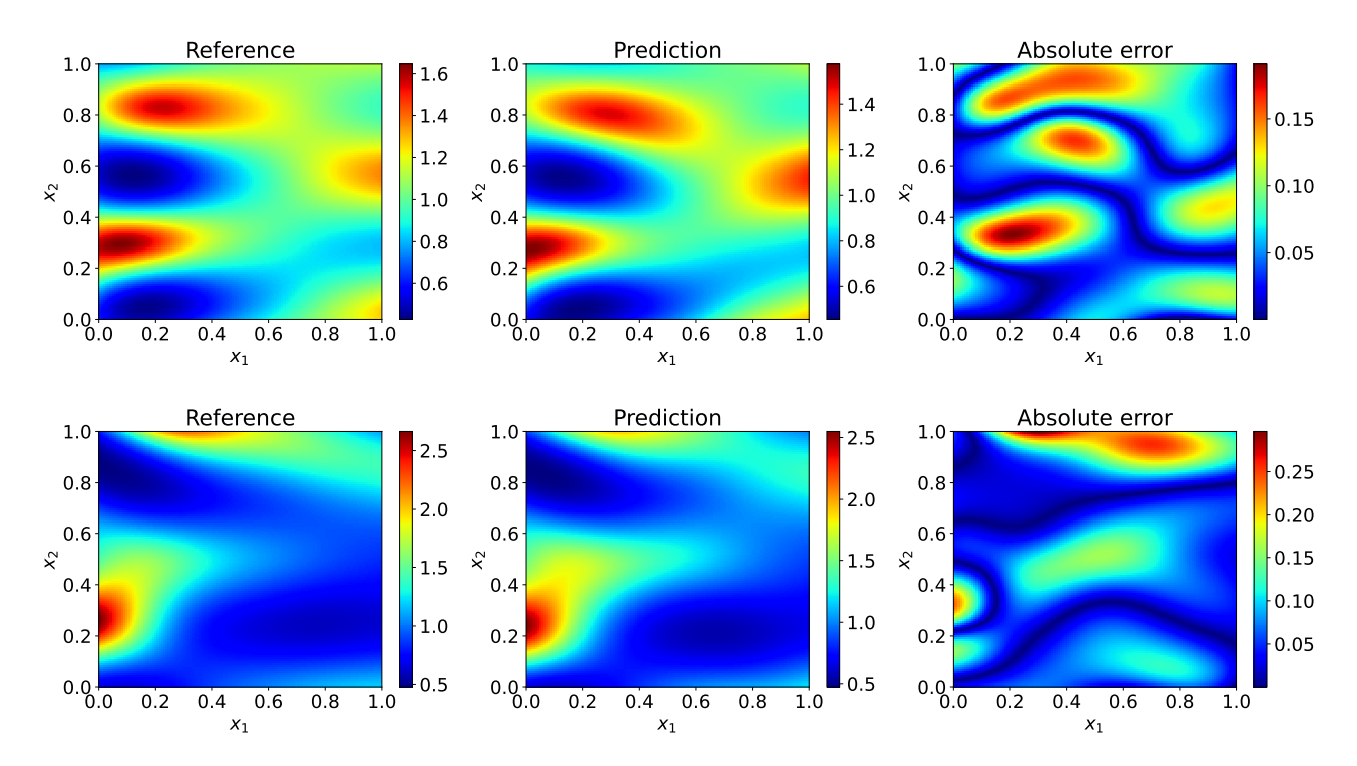


Fig. 9 Inverse map - Comparison of the reconstructed PDE-input (given the PDE-output/solution s) with the one predicted by the proposed invertible DeepONet and for Darcy type PDE.

addition can significantly improve the results for the inverse map. In Figure 10 we compare the ref-

Table 4 Relative errors on test data depending on the amount of labeled training data for the Darcy example with coarse-grained input parameters

erence solution for two illustrative test cases with the the forward map learned with labeled training data. As suggested by the cumulative results Table 4 the two predictions are very close to the reference and the accuracy is very high.

In Figures 11 and 12 the results for two illustrative inverse test case are shown. Due to the large difference in accuracy for the cases with and without labeled training data in Table 4 we present the results for both cases. In Figure 11 the results are shown for the training without labeled data. Whereas the main feature are captured, differences between predictions and reference are visible at some locations. For the case with labeled training data (Figure 12), these differences are

much smaller. The model is for both cases able to identify the CG input for unseen test data with a reasonable accuracy but for obvious reasons cannot capture the full, fine-grained parameter input but can nevertheless identify its coarse-grained features.

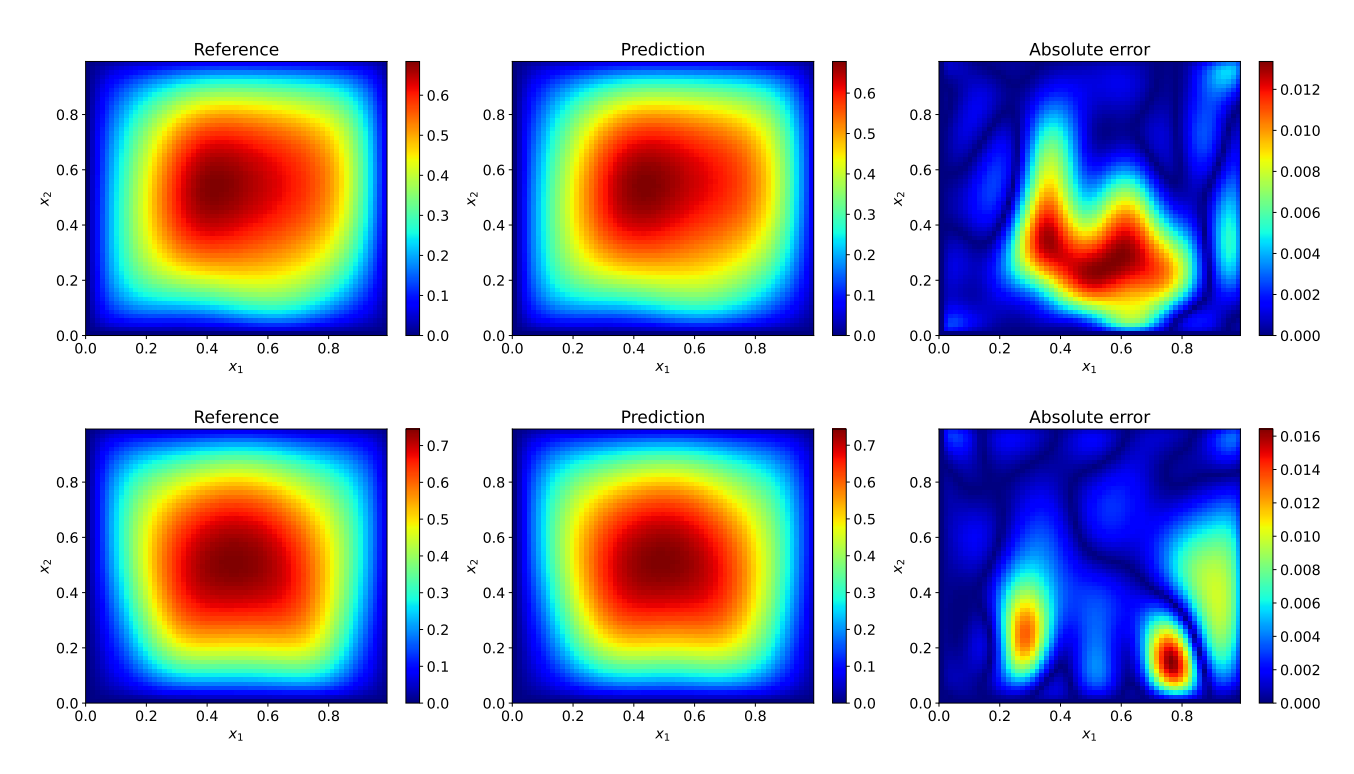


Fig. 10 Forward map - Comparison of the true PDE-output/solution s (given the coarse-grained PDE-input u) with the one predicted by the proposed invertible DeepONet and for Darcy type PDE.

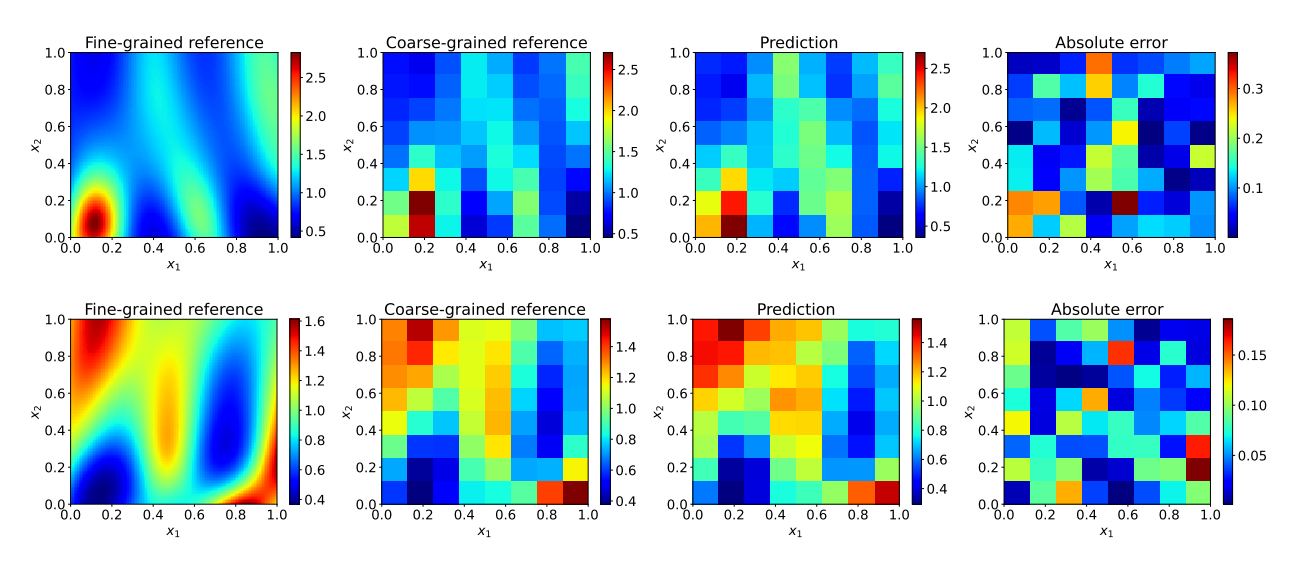


Fig. 11 Inverse map - Comparison of the coarse-grained PDE-input u (given the PDE-output/solution s) with the one predicted by the proposed invertible DeepONet and for Darcy type PDE with zero labeled training data.

3.4 Bayesian Inverse Problems

In this section we applied the aforementioned surrogates to Bayesian inverse problems using our novel algorithm to obtain an approximate posterior without the need for any costly sampling.

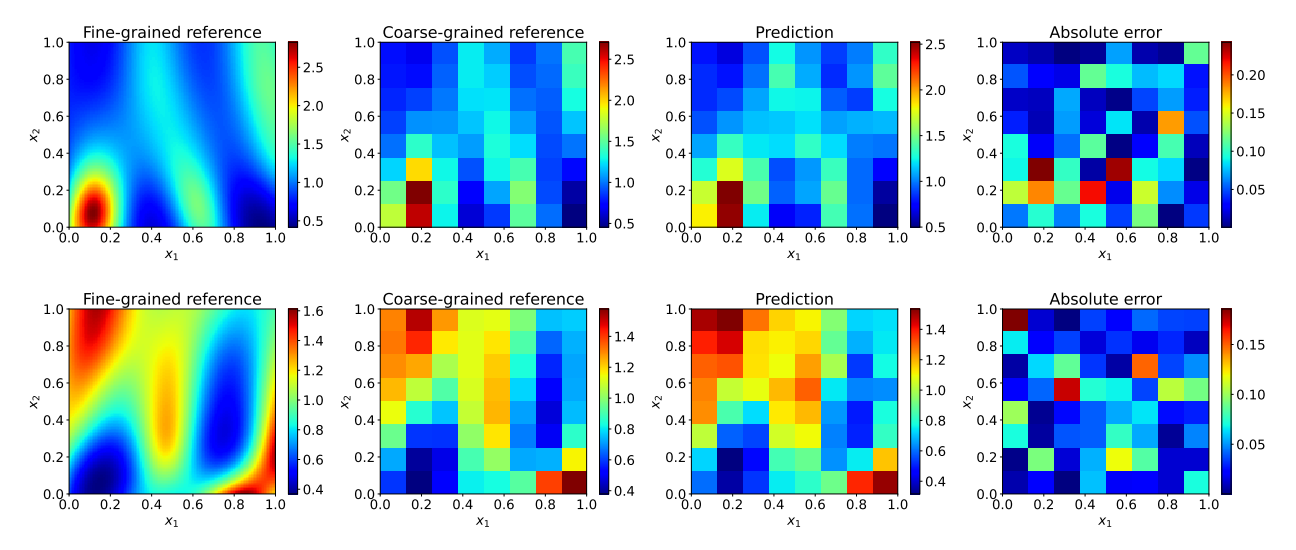


Fig. 12 Inverse map - Comparison of the coarse-grained PDE-input (given the PDE-output/solution s) with the one predicted by the proposed invertible DeepONet and for Darcy type PDE.

3.4.1 Reaction-Diffusion

Based on our trained model of the reaction-diffusion system (with 10percent labeled training data), we computed an approximate posterior based on the algorithm presented in the section 2.5 and compared it with the true parameter input for the test data. For the Gaussian mixture models involved for the prior and subsequently the posterior on \boldsymbol{b} we used two mixture components i.e. M=2 in Equations (27), (28). As prior $p(\boldsymbol{u})$ we again employed a Gaussian Process with zero mean and exponential quadratic covariance kernel with a length scale l=0.2 The results can be seen in the following Figures. The obtained posterior encapsulates the true parameter input for all three cases.

In Figure 13 we used test cases with 100 observed solution data points for each parameter input and a noise level of $\sigma^2 = 0.001$ (see Equation 23). In Figure 14 we increased the noise level and subsequently the uncertainty of our posterior is higher. This is as expected. In Figure 15 we again choose the original noise level but no decreased the number of observed solution data points to 25 points. Again the uncertainty of our posterior is increased.

Our method can therefore be used as a fast approach without any need for optimization and MCMC sampling to generate an approximate posterior. We note that the uncertainty increases if less data is observed and if σ increases. We note

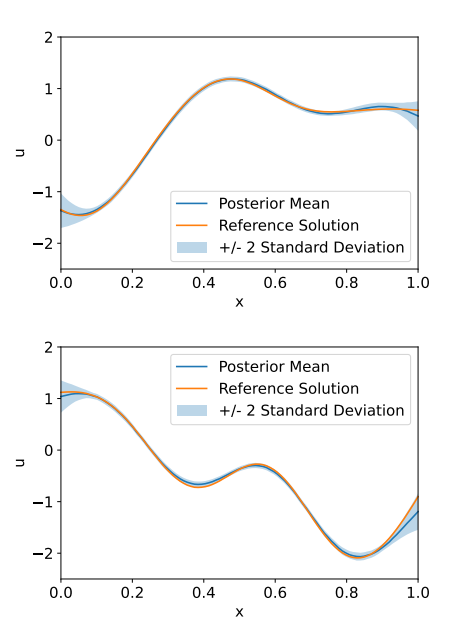


Fig. 13 Bayesian Inverse Problem: 100 observed data points with $\sigma^2 = 0.001$ and a 100-dimensional parameter input.

that we can also shown that our obtained approximate posterior does not only encapsulate the true parameter input but is also close to the actual posterior which can be computed using MCMC algorithms. For more details we refer to Appendix B.

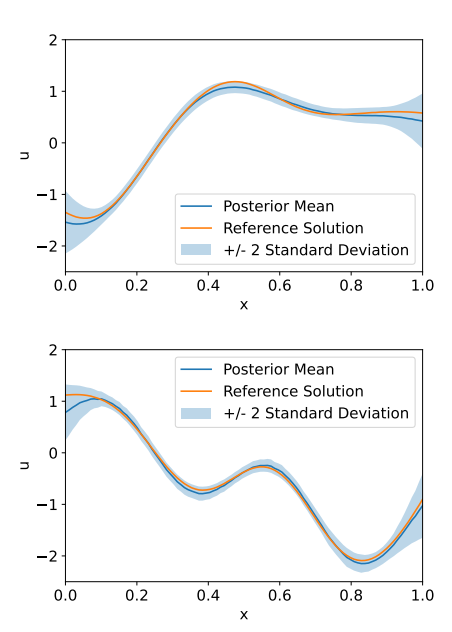


Fig. 14 Bayesian Inverse Problem: 100 observed data points with $\sigma^2=0.01$ and a 100-dimensional parameter input.

3.4.2 Darcy

We also solved Bayesian Inverse Problems in the context of the Darcy-type PDE by using our trained model of section 3.3 with added labeled training data. We computed an approximate posterior based on the algorithm presented in the section 2.5 and compared it with the true parameter input for the test data. For the Gaussian mixture models involved for the prior and subsequently the posterior on \boldsymbol{b} we used two mixture components i.e. M=2 in Equations (27), (28).

Firstly, we again assumed to have feature coefficients as inputs u for our model, which are defined as described in Section 3.3. The results can be seen in the following Figures. The obtained posterior mean and standard deviation are in good accordance with the actual reference solution, e.g. the parameter input used to generate the data. In Figure 16 we used test cases with 3844, e.g. a 62×62 grid, observed solution data points for each parameter input and a noise level of $\sigma^2 = 0.01$ (see Equation 23). In Figure 17 we decreased the noise level and subsequently the uncertainty of our posterior is lower and the posterior mean is closer to the actual reference. In Figure 18 we again choose the previous noise level but no decreased the number of observed solution data points to

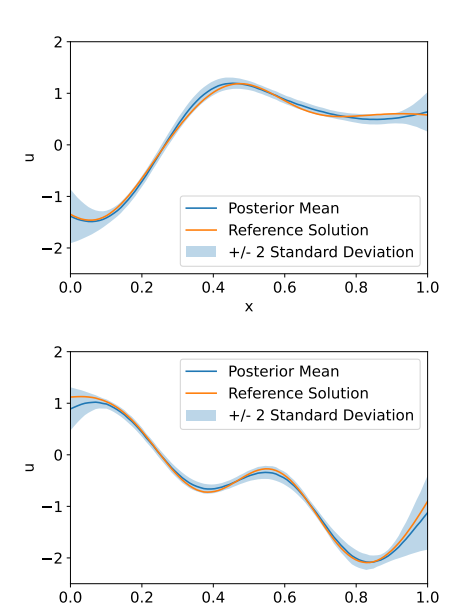


Fig. 15 Bayesian Inverse Problem: 25 observed data points with $\sigma^2 = 0.001$ and a 100-dimensional parameter input.

half the previous amount. Here the uncertainty of our posterior is increased.

Moreover, we also assumed to have coarse-grained inputs \boldsymbol{u} for our model, which are defined as described in Section 3.3.1. The results can be seen in the following Figures. The obtained posterior mean and standard deviation are again in good accordance with the actual reference solution, e.g. the parameter input used to generate the data.

In Figure 19 we used test cases with 3844, e.g. a 62×62 grid, observed solution data points for each parameter input and a noise level of $\sigma^2 = 0.01$ (see Equation 23). In Figure 20 we decreased the noise level and subsequently the uncertainty of our posterior is lower and the posterior mean is closer to the actual reference. In Figure 21 we again choose the previous noise level but no decreased the number of observed solution data points to half the previous amount. Here the uncertainty of our posterior is increased.

The trained surrogates can also for the Darcytype PDE be used to generate approximate posteriors in a very fast and efficient way. We were able to get good results for both feature coefficients

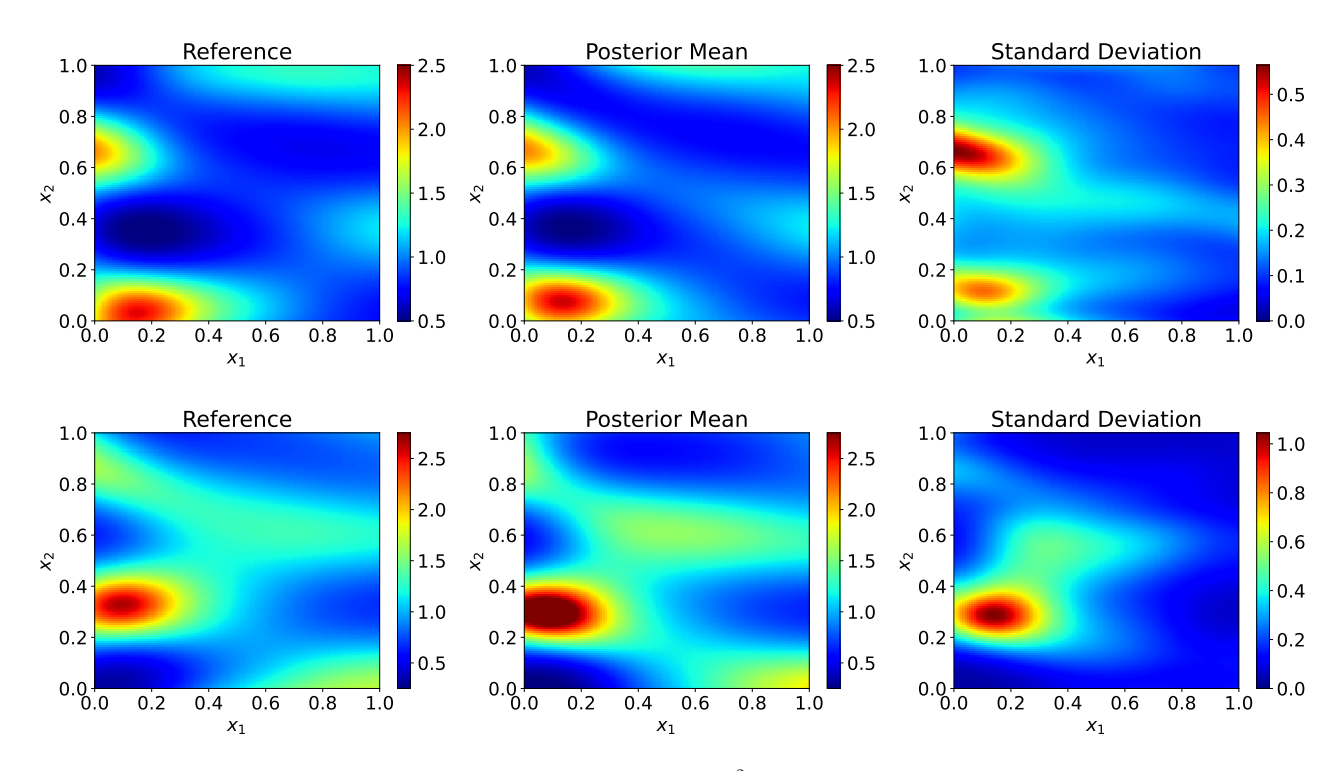


Fig. 16 Bayesian Inverse Problem: 3844 observed data points with $\sigma^2 = 0.01$ and a 64-dimensional parameter input representing feature coefficients.

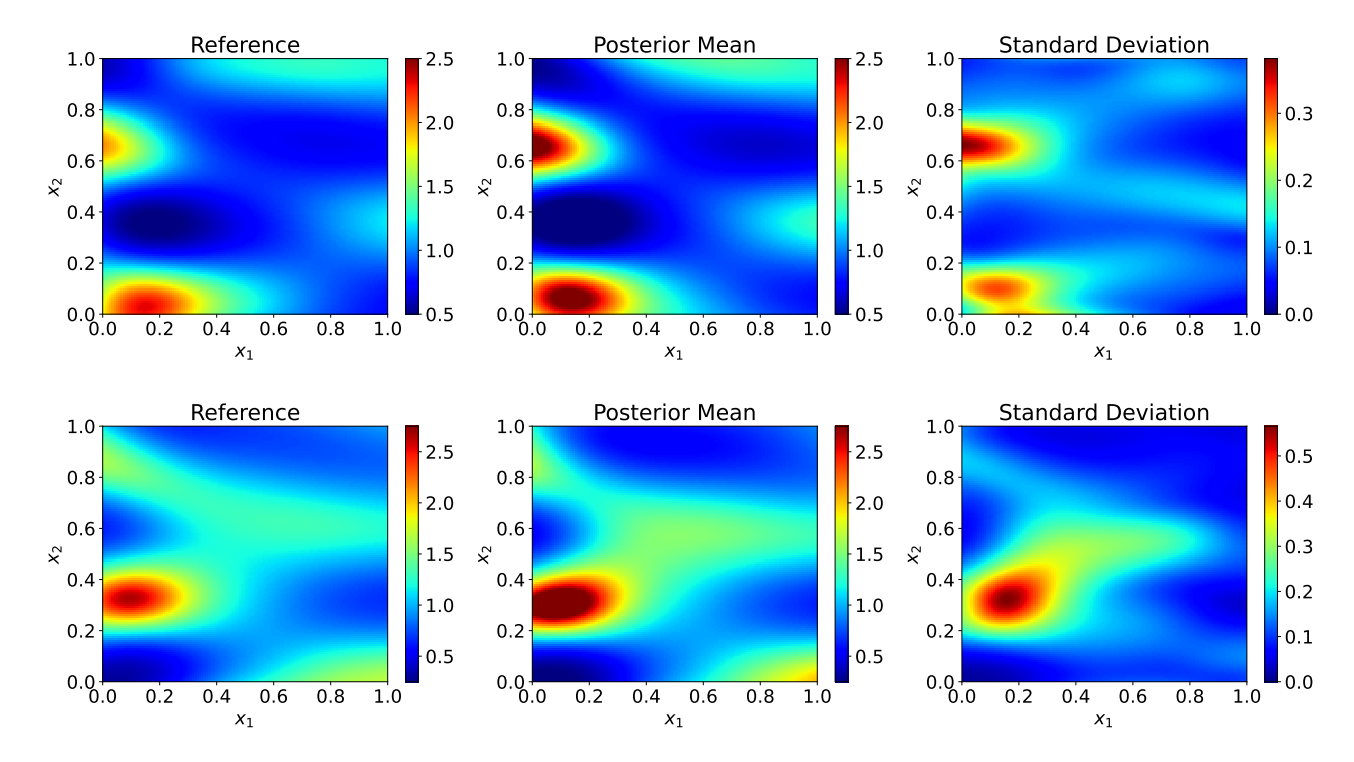


Fig. 17 Bayesian Inverse Problem: 3844 observed data points with $\sigma^2 = 0.001$ and a 64-dimensional parameter input representing feature coefficients.

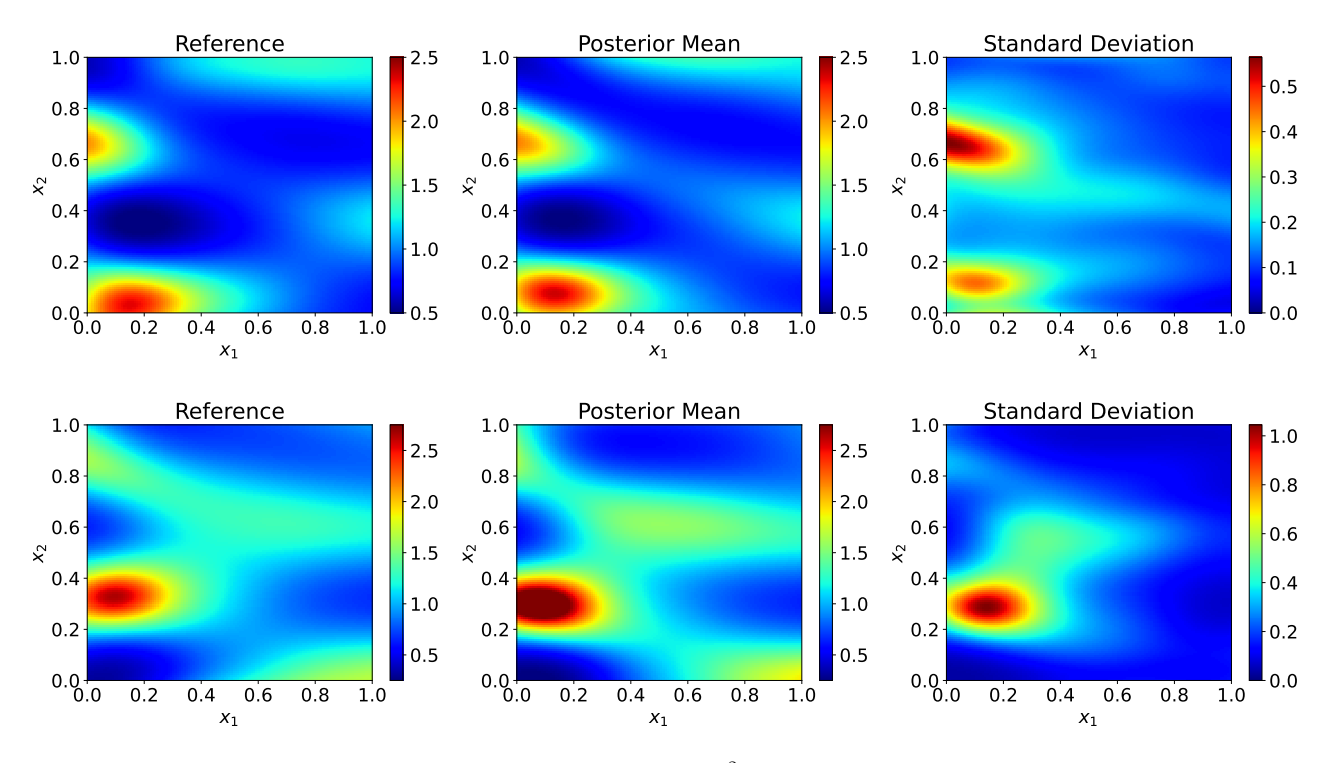


Fig. 18 Bayesian Inverse Problem: 1922 observed data points with $\sigma^2 = 0.01$ and a 64-dimensional parameter input representing feature coefficients.

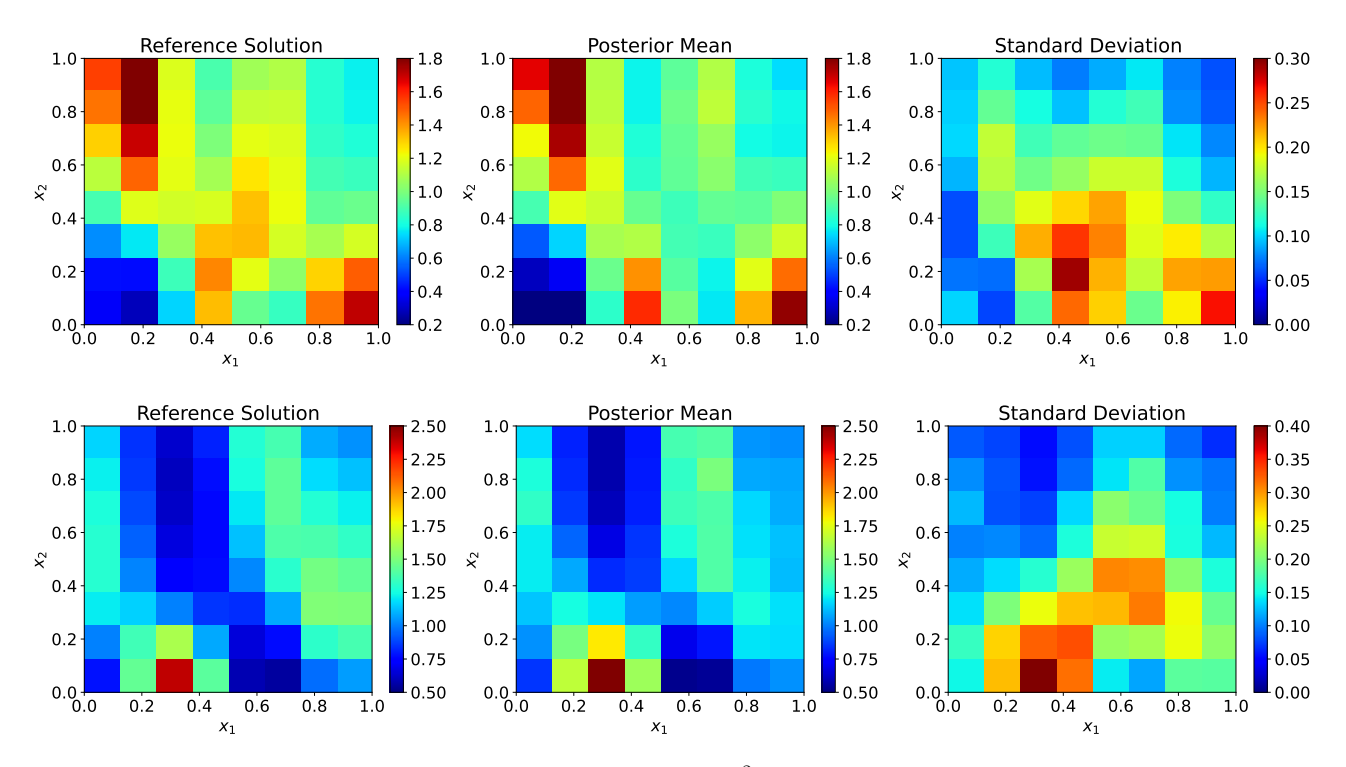


Fig. 19 Bayesian Inverse Problem: 3844 observed data points with $\sigma^2 = 0.01$ and a 64-dimensional, coarse-grained parameter input.

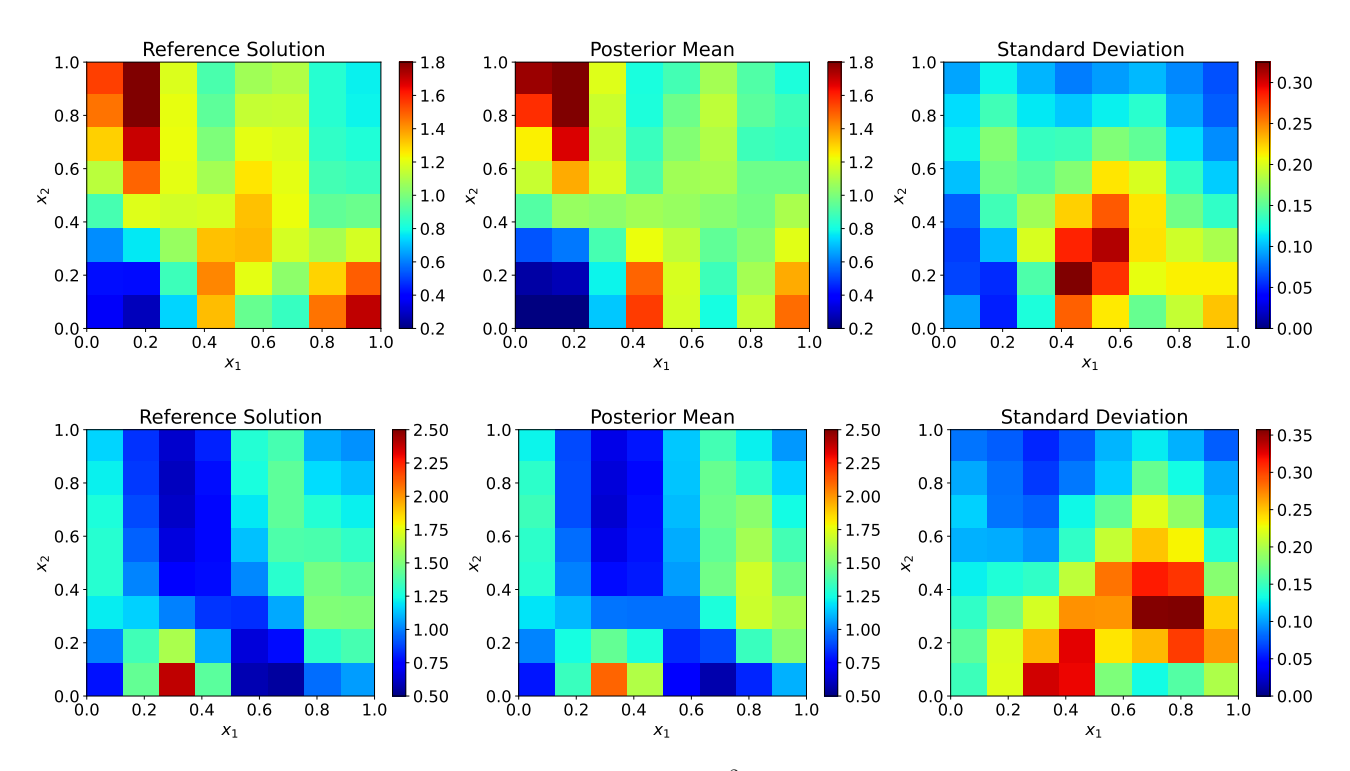


Fig. 20 Bayesian Inverse Problem: 3844 observed data points with $\sigma^2 = 0.001$ and a 64-dimensional parameter input representing feature coefficients.

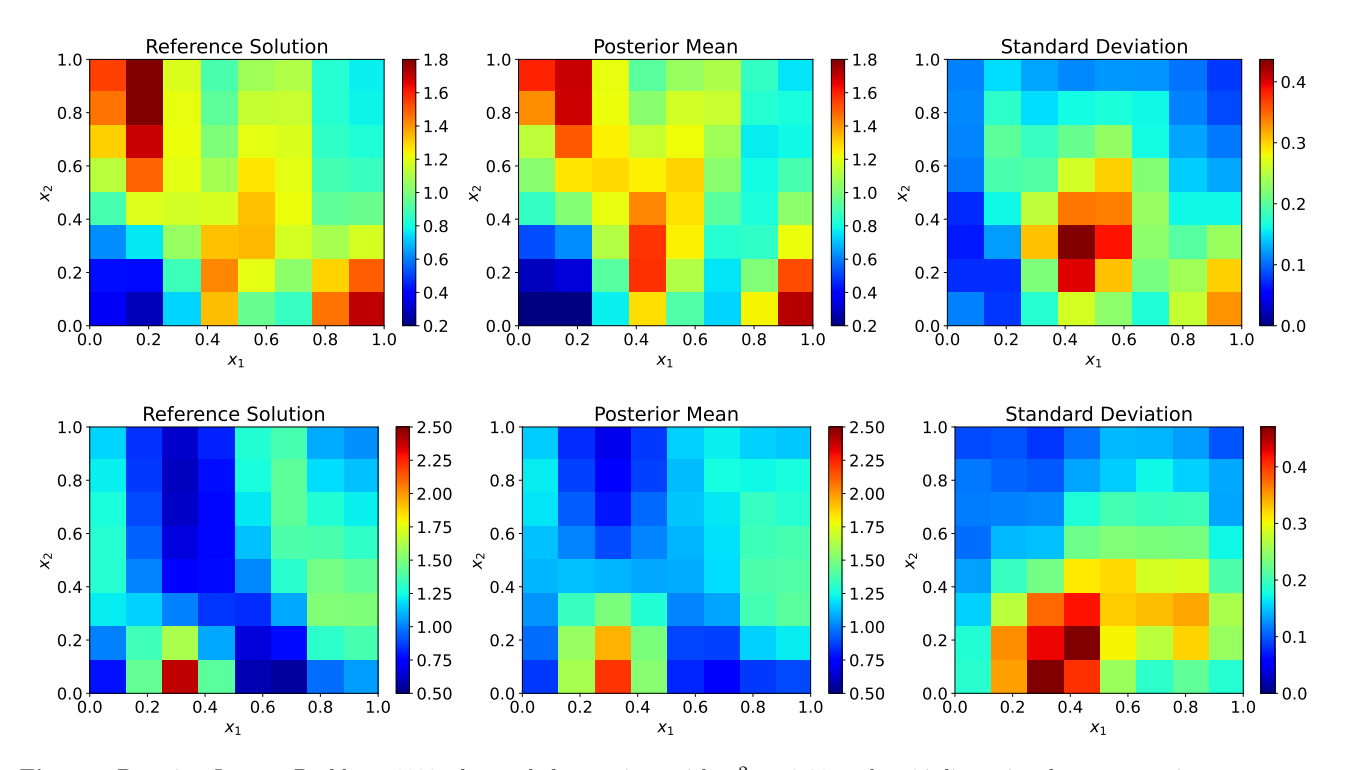


Fig. 21 Bayesian Inverse Problem: 1922 observed data points with $\sigma^2 = 0.01$ and a 64-dimensional parameter input representing feature coefficients.

as inputs and coarse-grained inputs. For the latter, we can however obviously only calculate the posterior for these coarse-grained inputs.

4 Conclusions

We introduced an invertible DeepONet architecture which efficiently approximates both forward and inverse operators with the same neural network. Once trained, it can be used to solve Bayesian inverse problems by generating an approximation to the posterior distribution without the need for additional, costly evaluations of the underlying model.

The performance of the proposed strategy was demonstrated on the anti-derivative operator, a reaction-diffusion PDE as well as a Darcy-type PDE and for all three cases small predictive errors were attained even with small amounts of expensive, labeled data. As one would expect, the inclusion of more labeled training data increased the predictive accuracy.

Due to invertibility of our architecture, the model is especially useful for Bayesian inverses problems as we can obtain a posterior distribution and samples from this distribution without the need of any costly MCMC runs and additional model evaluations. Given a reasonable accurate surrogate we were able to generate accurate posterior distribution for various amounts of given test data and model uncertainties. Therefore in our opinion the proposed model has large potential in all application examples where multiple Bayesian inverse problems need to be solved, as after one initial training phase the Bayesian inverse problems can be fast and accurate solved by the obtained surrogate.

A Influence of the amount of data

We show here the results of our algorithm for the antiderivative example for different amount of training data. We choose exactly the same settings as described in Section 3.1 and varied only the amount of labeled and unlabeled training data. In Figure 22 we plotted the relative error with regards to the amount of unlabeled training data. The color indicates the amount of labeled training data used, blue curves correspond to 1% added labeled training data, whereas red curves correspond to 100% added labeled training data.

We observe that the relative errors decrease if more labeled or unlabeled training data are added.

B Comparison with MCMC

Our method enables the efficient computation of a posterior distribution based on noisy test data. In the main part of this article we already showed that the true parameter input is encapsulated by the posterior. Here, we moreover show that the obtained posterior itself is also very similar to a posterior obtained by MCMC.

Therefore we computed for two, illustrative, randomly-chosen cases in the reaction-diffusion example the true posterior using the NUTS sampler from the Blackjax library and compared it with the posterior generated from our model. As is the case with all MCMC-based inference schemes, these provide the reference posterior (asymptotically). The results are shown in Figure 23.

References

Adler J, Öktem O (2017) Solving ill-posed inverse problems using iterative deep neural networks. Inverse Problems 33(12):124,007

Ardizzone L, Kruse J, Wirkert S, et al (2018) Analyzing inverse problems with invertible neural networks. arXiv preprint arXiv:180804730

Behrmann J, Grathwohl W, Chen RTQ, et al (2019) Invertible residual networks. ICML

Beskos A, Girolami M, Lan S, et al (2017) Geometric MCMC for infinitedimensional inverse problems. Journal

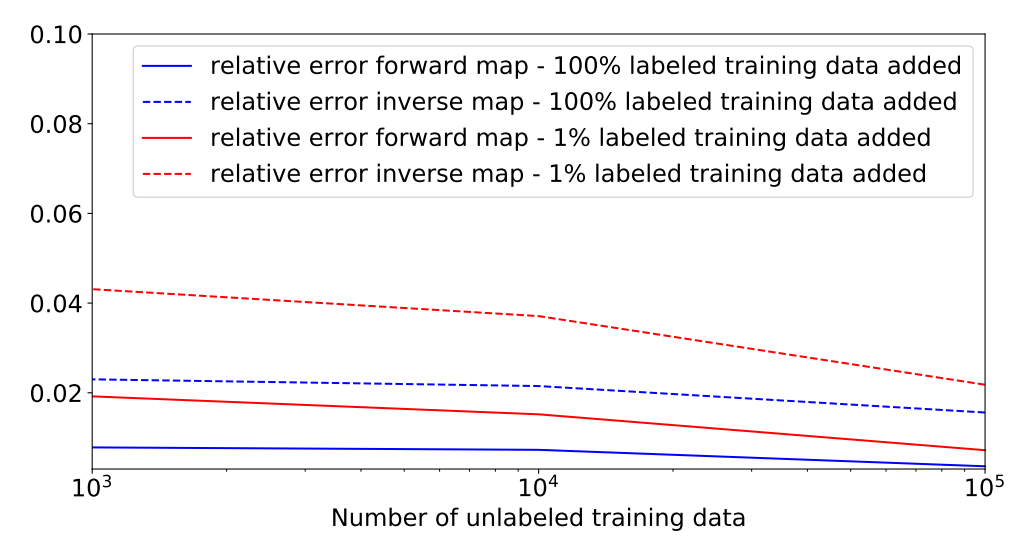


Fig. 22 relative errors on test data for the forward and inverse map depending on the amount of labeled and unlabeled training data

of Computational Physics 335:327–351. https://doi.org/10.1016/j.jcp.2016.12.041, URL https://www.sciencedirect.com/science/ article/pii/S0021999116307033

Bhattacharya K, Hosseini B, Kovachki NB, et al (2020) Model reduction and neural networks for parametric PDEs. arXiv preprint arXiv:200503180

Bradbury J, Frostig R, Hawkins P, et al (2018) JAX: composable transformations of Python+NumPy programs. URL http://github.com/google/jax

Champion KP, Brunton SL, Kutz JN (2019) Discovery of nonlinear multiscale systems: Sampling strategies and embeddings. SIAM Journal on Applied Dynamical Systems 18(1):312–333

Detommaso G, Cui T, Marzouk Y, et al (2018) A Stein variational Newton method. In: Advances in Neural Information Processing Systems, pp 9169–9179

Dinh L, Sohl-Dickstein J, Bengio S (2016) Density estimation using Real NVP. arXiv preprint arXiv:160508803

Gin C, Lusch B, Brunton SL, et al (2019) Deep learning models for global coordinate transformations that linearize pdes. arXiv preprint arXiv:191102710

Hoffman MD, Blei DM, Wang C, et al (2013) Stochastic variational inference. The Journal of Machine Learning Research 14(1):1303–1347

Kalia M, Brunton SL, Meijer HG, et al (2021) Learning normal form autoencoders for data-driven discovery of universal, parameterdependent governing equations. arXiv preprint arXiv:210605102

Kaltenbach S, Koutsourelakis PS (2020) Incorporating physical constraints in a deep probabilistic machine learning framework for coarse-graining dynamical systems. Journal of Computational Physics 419:109,673

Kaltenbach S, Koutsourelakis PS (2021) Physicsaware, probabilistic model order reduction with guaranteed stability. ICLR

Karnakov P, Litvinov S, Koumoutsakos P (2022) Optimizing a DIscrete loss (ODIL) to solve forward and inverse problems for partial differential equations using machine learning tools. arXiv preprint arXiv:220504611

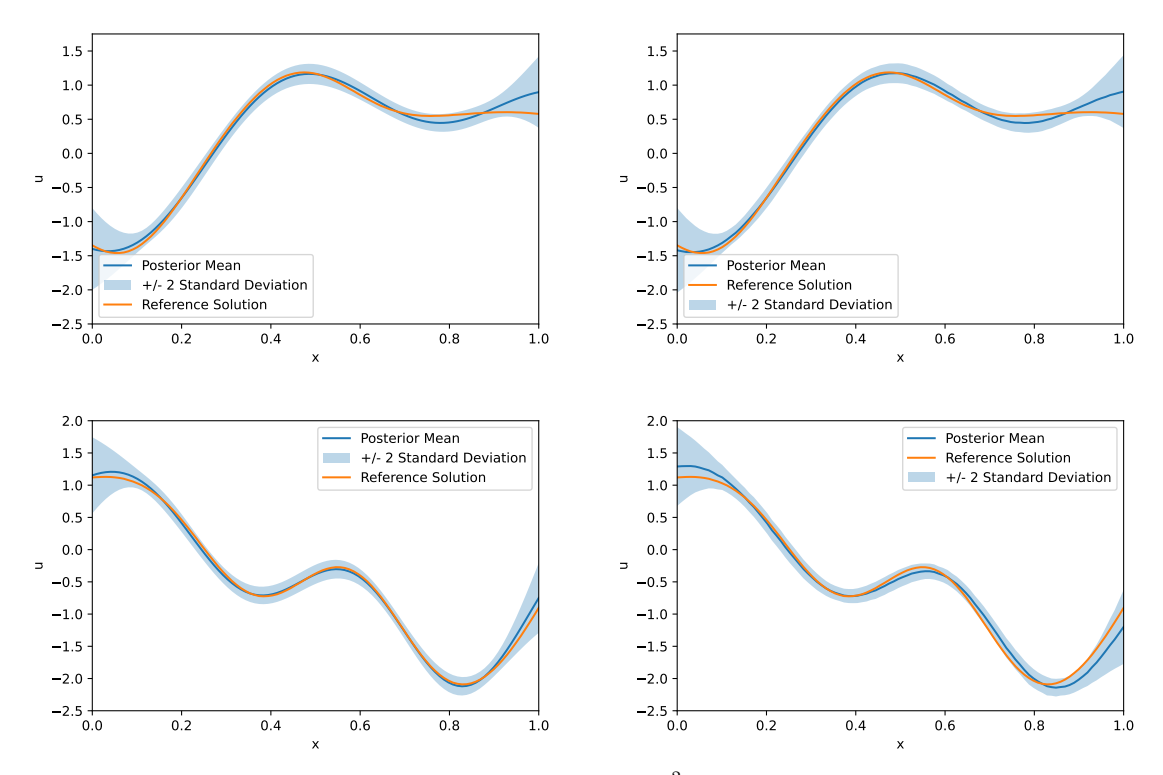


Fig. 23 Bayesian Inverse Problem: 100 observed data points with $\sigma^2 = 0.01$ and a 100-dimensional parameter input. Left: Posterior based on MCMC (NUTS), Right: Posterior obtained by our algorithm

Kingma DP, Ba J (2014) Adam: A method for stochastic optimization. arXiv preprint arXiv:14126980

Kissas G, Seidman J, Guilhoto LF, et al (2022) Learning operators with coupled attention. arXiv preprint arXiv:220101032

Klus S, Nüske F, Koltai P, et al (2018) Data-Driven Model Reduction and Transfer Operator Approximation. Journal of Nonlinear Science 28(3):985–1010. https://doi.org/10.1007/s00332-017-9437-7, URL https://doi.org/10.1007/s00332-017-9437-7

Koopman BO (1931) Hamiltonian Systems and Transformations in Hilbert Space. Proceedings of the National Academy of Sciences of the United States of America 17(5):315–318. URL https://www.jstor.org/stable/86114

Koutsourelakis P (2009) A multi-resolution, non-parametric, Bayesian framework for identification of spatially-varying model parameters. Journal of Computational Physics 228(17):6184-6211

Koutsourelakis P, Zabaras N, Girolami M (2016) Big data and predictive computational modeling. JCoPh 321:1252–1254

Lagaris IE, Likas A, Fotiadis DI (1998) Artificial neural networks for solving ordinary and partial differential equations. IEEE transactions on neural networks 9(5):987–1000

Lee K, Carlberg KT (2020) Model reduction of dynamical systems on nonlinear manifolds using deep convolutional autoencoders. Journal of Computational Physics 404:108,973

Li Z, Kovachki N, Azizzadenesheli K, et al (2020) Fourier neural operator for parametric partial differential equations. arXiv preprint arXiv:201008895

- Logg A, Mardal KA, Wells G (2012) Automated solution of differential equations by the finite element method: The FEniCS book, vol 84. Springer Science & Business Media
- Lu L, Jin P, Pang G, et al (2021) Learning nonlinear operators via DeepONet based on the universal approximation theorem of operators. Nature Machine Intelligence 3(3):218–229
- Raissi M, Perdikaris P, Karniadakis GE (2019) Physics-informed neural networks: A deep learning framework for solving forward and inverse problems involving nonlinear partial differential equations. Journal of Computational Physics 378:686-707
- Sander ME, Ablin P, Blondel M, et al (2021) Momentum residual neural networks. arXiv 210207870
- Wang S, Wang H, Perdikaris P (2021) Learning the solution operator of parametric partial differential equations with physics-informed deeponets. arXiv preprint arXiv:210310974